

A machine learning approach to crater detection from topographic data

Kaichang Di^a, Wei Li^{a,b}, Zongyu Yue^{a,*}, Yiwei Sun^{a,b}, Yiliang Liu^{a,b}

^a State Key Laboratory of Remote Sensing Science, Institute of Remote Sensing and Digital Earth, Chinese Academy of Sciences, Beijing 100101, PR China

^b University of Chinese Academy of Sciences, Beijing 100049, PR China

Received 7 December 2013; received in revised form 21 May 2014; accepted 19 August 2014

Available online 3 September 2014

Abstract

Craters are distinctive features on the surfaces of most terrestrial planets. Craters reveal the relative ages of surface units and provide information on surface geology. Extracting craters is one of the fundamental tasks in planetary research. Although many automated crater detection algorithms have been developed to extract craters from image or topographic data, most of them are applicable only in particular regions, and only a few can be widely used, especially in complex surface settings. In this study, we present a machine learning approach to crater detection from topographic data. This approach includes two steps: detecting square regions which contain one crater with the use of a boosting algorithm and delineating the rims of the crater in each square region by local terrain analysis and circular Hough transform. A new variant of Haar-like features (scaled Haar-like features) is proposed and combined with traditional Haar-like features and local binary pattern features to enhance the performance of the classifier. Experimental results with the use of Mars topographic data demonstrate that the developed approach can significantly decrease the false positive detection rate while maintaining a relatively high true positive detection rate even in challenging sites.

© 2014 COSPAR. Published by Elsevier Ltd. All rights reserved.

Keywords: Crater detection algorithm; Topographic data; Machine learning; AdaBoost; Martian surface

1. Introduction

Impact craters are distinctive features on most terrestrial planets and are usually formed by the collision of comets or asteroids with celestial body surfaces. The distributions and morphologies of craters are closely related to the geology and surface characteristics of planets. Craters can survive a long geologic time if the surface erosion rate is very slow; heavily cratered surfaces are relatively older than less cratered surfaces in general. Crater density, which is derived from the size of the crater over the area of the covered region, is therefore important in planetary research and

has been widely utilised to determine the relative chronologies of different planetary surfaces (Tanaka, 1986; Hartmann and Neukum, 2001; Haruyama et al., 2009; Morota et al., 2009). The extraction and counting of craters are critical to obtain accurate geologic ages; however, most researchers have manually done this work thus far (Barlow, 1988; Kuzmin et al., 1989; Costard, 1989; Rodionova et al., 2000; Robbins and Hynek, 2012). Although manual extraction can relatively give detailed information on craters exposed on planetary surfaces, it is generally a time-consuming and laborious task, and it can be biased by the researcher's personal knowledge and skills. The data sources employed in manual extraction also affect crater extraction. For example, the published Martian crater catalogue by Barlow (1988; hereafter referred to as the Barlow catalogue) utilised Viking images of 42,284 craters extracted from the entire Martian surface.

* Corresponding author.

E-mail addresses: kcdi@irsa.ac.cn (K. Di), liwei@irsa.ac.cn (W. Li), yuezy@irsa.ac.cn (Z. Yue), sunyw@irsa.ac.cn (Y. Sun), yliu@irsa.ac.cn (Y. Liu).

The new version of the Martian crater database by Robbins and Hynek (2012; hereafter referred to as the Robbins catalogue) includes 384,343 craters extracted from high-resolution images of the Thermal Emission Imaging System. More craters are expected to be found in the near future in new Martian images with high resolutions, and laborious work may need to be done to obtain a new version of the crater catalogue. Therefore, developing a robust crater detection algorithm (CDA) is significant in planetary research.

Numerous CDAs have been developed in the past because of the importance of crater detection. Salamunićcar et al. (2011) tabulated 77 various CDA approaches previously published, and these approaches can be divided into image-based and digital elevation model (DEM)-based methods according to data source. Image-based CDAs are developed in various ways, including circle fitting (Honda et al., 2000; Cheng et al., 2003; Magee et al., 2003; Sawabe et al., 2006; Luo et al., 2011; Salamunićcar et al., 2011), highlight and shadow region matching (Urbach, 2007; Urbach and Stepinski, 2009), template matching (Flores-Méndez, 2003; Bandeira et al., 2007a,b), object-oriented method (Yue et al., 2008), texture analysis (Barata et al., 2004), machine learning (Burl et al., 2001; Vinogradova et al., 2002; Wetzler et al., 2005; Martins et al., 2009; Stepinski et al., 2012) and combined methods with two or more of the above algorithms (Honda et al., 2002; Ding et al., 2011; Bandeira et al., 2012; Meng et al., 2013; Cohen and Ding, in press). Another type of CDA is based on DEM data, and it is not affected by sunlight and is more suitable to crater detection than to images to a certain extent. Current global high-resolution DEM data are available for several planets (e.g. Mars and the Moon), and many researchers have proposed various CDAs on the basis of DEM data. Some previous works (Bue and Stepinski, 2007; Stepinski et al., 2007; Salamunićcar and Lončarić 2008a,b, 2010; Salamunićcar et al., in press) adopted the edge detection method to identify craters on DEM data, and the method employed is similar to that used in previous image-based CDAs. Other studies (e.g. Stepinski et al., 2009) developed algorithms to identify craters as round-shaped depressions of a certain depth from DEM data. The object-oriented classification method has been recently utilised to extract lunar impact craters from Chang'E-1 satellite DEM data (Wan et al., 2012). Hough transform has been applied in global detection of large lunar craters (≥ 10 km in diameter) from the CE-1 DEM (Luo et al., 2013). Other strategies, such as computing the shape characteristics of elevation contour lines (Yue et al., 2013), have also been developed to extract craters from DEM data. However, some flaws in the above DEM-based CDAs exist, especially in the cases of deeply degraded, overlapped or nested craters. The high false detection rate is a major problem in most previous CDA methods.

In this study, we present a DEM-based CDA which uses machine learning to significantly decrease the false positive

detection rate while maintaining a high true positive detection rate. Some effective features of image-based object detection, such as Haar-like features and local binary pattern (LBP) features, are adopted for crater detection in DEM data for the first time. We also propose a new variant of Haar-like features (scaled Haar-like features) to enhance our method. Experimental results show that the proposed method effectively performs in crater extraction from DEM data even in challenging sites.

2. Data and method

The DEM data employed in this research are obtained from the Mars GIS DVD v. 1.7 data set, which can be downloaded from the USGS website (<ftp://pdsimage2.wr.usgs.gov/pub/pigpen/mars/mola/>). The product name in the dataset is 'mola128_88Nto88S_Simp_clon0'. These near-global DEM data were generated from the Mars Orbiter Laser Altimeter (MOLA) with a resolution of 463.0836 m at the equator. The data are in equidistant cylindrical projection centred at (0°, 0°). Fig. 1 shows the DEM map with four rectangular regions marked by numbers and letters. The regions marked by numbers are the test sites for our method, and the regions marked by letters are the sample regions from which the training samples are selected for the machine learning algorithm. These four regions are located in the low-latitude region of Mars, which has a relatively small distortion on the cylindrical-projected DEM. Section 4.1 presents the detailed information on the test sites.

The diagram of the proposed CDA is shown in Fig. 2. It consists of two main steps: (1) detecting square regions which contain one crater with the use of a boosting algorithm which uses Haar-like, scaled Haar-like and LBP features; and (2) delineating the crater rim in the square region by local terrain analysis and circular Hough transform (CHT).

3. Detection of crater regions on the DEM

The detection of crater regions on the DEM can be formulated as a pattern recognition problem. The information extracted from different locations in the DEM is assigned to one of two classes: crater or non-crater. Our method is based on the AdaBoost machine learning approach developed by Viola and Jones (2001). The approach achieved excellent results in the field of face detection and has also been successfully applied in image-based crater detection (Martins et al., 2009; Bandeira et al., 2012). In this study, we expand this approach to make it suitable to detecting craters in DEM.

3.1. Sample data preparation and feature extraction

The first step of this approach is to prepare a training set of positive and negative samples of craters. In this research, 1046 square blocks centred at the crater centres were

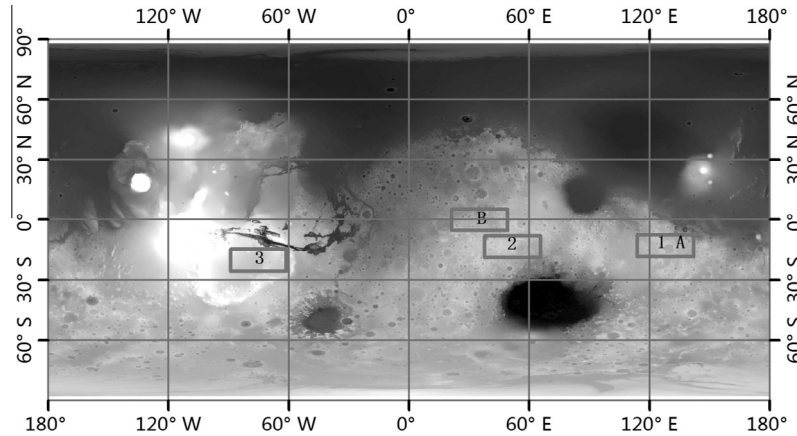


Fig. 1. DEM map of the MOLA data. The regions marked by numbers are the test sites for our method, and the regions marked by letters are the sample regions from which the training samples are selected for the machine learning algorithm.

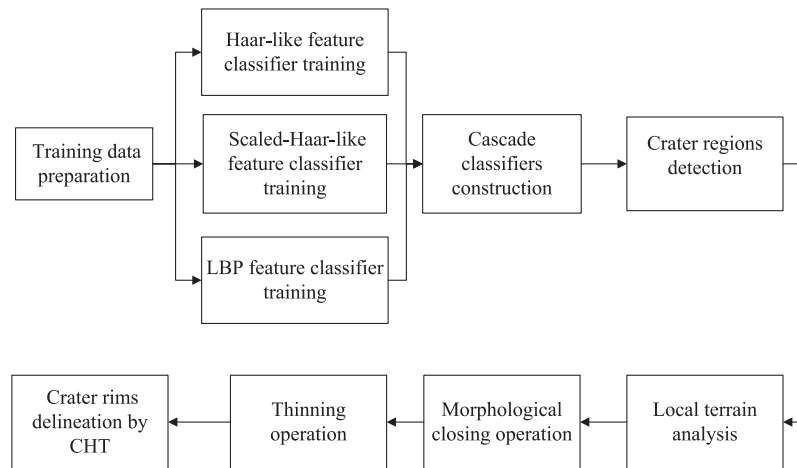


Fig. 2. Diagram of the proposed CDA.

extracted from the DEM data as positive samples. The widths of the blocks are 1.5 times that of the crater diameter. We also manually and randomly extracted 946 square blocks from the DEM data containing no craters as negative samples. All the samples are resampled to 20×20 pixels with the bilinear interpolation method. With the resolution of MOLA DEM considered, craters with a diameter greater than 6 km are selected on the basis of Robbins catalogue because the extracted DEM blocks with small craters contain a few features.

The second step of the approach is feature extraction in which three classes of features are calculated to train the algorithm. The first class is a Haar-like feature, and this class is the same as that used by Viola and Jones (2001). Haar-like features are obtained with a set of binary masks in which each mask is a rectangular region made up of two or more adjacent rectangles. By placing the binary masks with two types of rectangles (white and black) at different positions on the DEM data, we can obtain the feature value for a particular mask by subtracting the sum of pixel elevation values covered by the black rectangle from the

sum of pixel elevation values covered by the white rectangle. Haar-like features in the DEM describe the difference in elevation between two rectangles, and such a difference is similar to that in the greyscale values in an image. With block data with a size 20×20 , the derived set of rectangle features is quite large (typically thousands). Only eight types of square masks (Fig. 3) are used to extract features to decrease the computation of feature extraction. A total of 4714 features are obtained for each resized sample.

The second class of features is a variant of the first one, and it is called a scaled Haar-like feature. This feature is proposed on the basis of the fact that large craters are usually deeper than small craters, and this means most of the Haar-like feature values of large craters are larger than those of small craters. The scaled Haar-like feature is computed by division of the Haar-like feature value with a coefficient of the resolution of the sample to adjust the Haar-like features of large craters and small craters to the same scale. For example, if a $w \times w$ sample is selected in the first step with the original resolution of c and resized to $s \times s$ pixels, the Haar-like feature values of sample



Fig. 3. Eight types of masks used for Haar-like feature extraction.

$F = \{x_1, x_2, \dots, x_{4714}\}$ can be computed. The scaled Haar-like feature values of the sample would then be $C = F \cdot (c \cdot w/s)^{-1}$. It can be seen that the scaled Haar-like feature is actually a scaling of the elevation in vertical direction by considering the resolution of the DEM. The number of scaled Haar-like features for a sample is clearly the same as that of Haar-like features.

An LBP feature was first described by Ojala et al. (1994, 1996), and this is the third class of features which have been found to be powerful for texture classification in face recognition (Zhang et al., 2005; Liao et al., 2007). The original LBP operator labels the pixels of an image by thresholding of the 3×3 neighbourhood of each pixel with the centre value and by conversion of the result to a binary string or a decimal number. An extension to the basic LBP with respect to neighbourhoods of different sizes is the multi-scale LBP (Ojala et al., 2002). Fig. 4 illustrates the basic LBP and multi-scale LBP operator. In multi-scale LBP, the comparison operator between single pixels in LBP is replaced with a comparison between the average grey values of sub-regions. In our approach, all possible mask rectangles whose widths and heights are divisible by three are placed in the DEM block to calculate the LBP features. As a result, 3969 features for each resized sample are obtained. Although the sets of three classes of features are quite large, their computation can be extremely fast if an auxiliary integral image is built (Viola and Jones, 2004).

3.2. Training boosting classifier

Because of a large amount of features for a training set, a number of machine learning approaches (e.g. decision tree, support vector machines, maximum likelihood and neural networks) can be used to learn a classification function. In our approach, a variant of the AdaBoost algorithm (Viola and Jones, 2004) is utilised to select the features and train the classifier. This algorithm can efficiently solve three fundamental problems: selecting a small set of effective

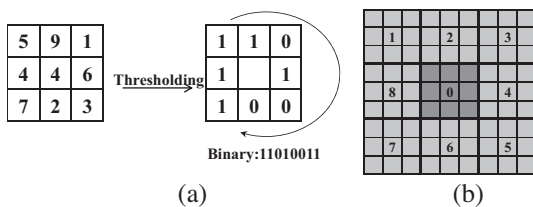


Fig. 4. LBP operator. (a) Basic LBP operator. The binary string 11010011 is obtained by coding the thresholding result clockwise from the top-left corner. (b) 9×9 Multi-scale LBP operator.

features from a large feature set, constructing weak classifiers on the basis of the selected features and boosting the weak classifiers into a strong classifier. In this training algorithm, a set of weak classifiers, each depending only on a single extracted feature, are combined to form a strong classifier. Each weak classifier is a single node classification and regression tree and can be simply represented as follows:

$$f(x, f, p, \theta) = \begin{cases} 1, & \text{if } p \cdot f(x) \geq p \cdot \theta \\ 0, & \text{otherwise} \end{cases} \quad (1)$$

where x is a DEM block to be classified, f is a specific feature value of x , $P \in \{-1, 1\}$ is a polarity indicating the direction of the inequality, and θ is a threshold; the result 1 means x is a crater and 0 means it is a non-crater. In practice, no single weak classifier can perform with a low error rate because a single feature is not enough for classification. However, the weak classifiers which can best separate the positive and negative samples can be selected to combine a strong classifier and can significantly improve classification performance. The main steps are described as follows:

- (1) All feature vectors are computed from each block for the training set of the DEM.
- (2) The weight $w_{1,i}$ is initialised for each training image with the following equation:

$$w_{1,i} = \begin{cases} \frac{1}{2m}, & \text{if } i \text{ is crater} \\ \frac{1}{2n}, & \text{if } i \text{ is noncrater} \end{cases} \quad (2)$$

where m is the number of craters, and n is the number of non-craters in the training set.

- (3) For $t = 1, \dots, T$, (T is a pre-defined number of weak classifiers), the following calculations are performed:
 - (a) The weights are normalised with Eq. (3) as follows:

$$w_{t,i} = \frac{w_{t,i}}{\sum_{j=1}^n w_{t,j}} \quad (3)$$

- (b) The weak classifier which minimises the weighted error is selected as follows:

$$\varepsilon_t = \min_{f, p, \theta} \sum_i w_{t,i} |h(x_i, f, p, \theta) - y_i| \quad (4)$$

- (c) $h_t(x) = h(x, f_t, p_t, \theta_t)$ is defined, where f_t , p_t and θ_t are the minimisers of ε_t .
 - (d) The weights are updated as follows:

$$w_{t+1,i} = w_{t,i} \beta_t^{1-e_i} \quad (5)$$

where $e_i = 0$ if x_i is correctly classified, $e_i = 1$ if x_i is incorrectly classified and

$$\beta_t = \varepsilon_t / (1 - \varepsilon_t) \quad (6)$$

- (4) The outputs of all weak classifiers are combined to build a strong classifier as follows:

$$H(x) = \begin{cases} \text{crater,} & \text{if } R = \sum_{t=1}^T \alpha_t \cdot h_t(x) - \frac{1}{2} \sum_{t=1}^T \alpha_t > 0 \\ \text{noncrater,} & \text{otherwise} \end{cases} \quad (7)$$

where $\alpha_t = \log(1/\beta_t)$.

The classification result R is a real number, whose sign represents the class, and its absolute magnitude is the ‘confidence’ of the decision. We should obtain the sign of R to determine the classification. R is compared with a threshold T to regulate the rate of false positive/false negative, and the sign of $(R - T)$ is taken to decide the class. Increasing T not only decreases the false positive rate (FPR) but also increases the false negative rate. We employed the GML AdaBoost Matlab toolbox (Vezhnevets, 2009) to train three classifiers based on the above three classes of features. The training results are shown in the following section. Fig. 5 shows one of the positive samples rendered in ArcGIS software. Fig. 6 shows the top six mask features selected from the training set which uses AdaBoost with Haar-like features, scaled Haar-like features and LBP features. The first selected feature in the Haar-like and scaled Haar-like features clearly appears to focus on detecting a hollow in the region centre. The other five features and LBP features are located at the edges of a crater, which were focused on finding the crater rims. We calculate the accuracy of the strong classifier in each loop of iteration to estimate the performance of the classifier in distinguishing the samples.

Fig. 7 shows the accuracy curves of the three classifiers. All of the three classifiers achieve an accuracy of nearly 0.9 even with only one feature, and both the scaled Haar-like and Haar-like feature classifiers can correctly distinguish all the samples when the number of iterations reaches 80. The LBP feature classifier can also correctly distinguish all the samples when the number of iterations reaches 100. All of the three classes of features are therefore effective in classifying the craters and non-craters in the training set.

Although the three strong classifiers can correctly classify training data, a high FPR still exists when we indi-

vidually apply them to detect craters in the test site. The false positive regions of the three classifiers are also different. The Haar-like classifier usually gives a false result by considering large noncrater regions as craters, whereas the scaled Haar-like classifier generally produces similar mistakes in small areas, and that indicates they can complement each other. Constructing a cascade of the three classifiers generates improved results. A cascade of classifiers means only the regions accepted by all of the classifiers are considered to be the true crater regions. We calculated the receiver operating characteristic (ROC) curves (Fawcett, 2004) of the three classifiers and the cascade classifier to compare the classifiers (Fig. 8). The ROC space is defined by an FPR and the true positive rate (TPR) as the x and y axes, respectively. This space depicts the relative trade-offs between true positives and false positives as the threshold T changes. Both the number of training iterations and the threshold T can affect the detecting result. We set the number of iterations at 400 and the threshold T at 0.12 for the Haar-like classifier, 0.01 for the scaled Haar-like classifier and 0.05 for the LBP classifier to decrease the FPR (i.e. keeping the evaluation factor B at approximately 0.15, which is introduced in Section 5). The resultant ROC curves are shown in Fig. 8. The curves show that the cascade classifier always performs better than the three single-feature classifiers, i.e., the cascade classifier achieves a lower FPR than the three single-feature classifiers when reaching the same TPR, or it achieves a higher TPR than the three single-feature classifiers when maintaining the same FPR.

It is worth mentioning that we also calculated other preformation measures such as F1, precision, and recall. They show the same trend as that of ROC in Fig. 8: the cascade of the three classifiers performs the best, i.e., better than the three single-feature classifiers.

3.3. Detecting crater regions

Sliding a detection window in the DEM data determines the crater regions after the classifiers are trained. The classifiers can detect craters of different sizes in two ways: resizing the detection window or resizing the DEM data. In our method, we resize the DEM data by building a pyramid from it, in which the size of each layer is decreased to 1.2^{-1} times the size of the previous layer. The bottom layer in the pyramid is the original DEM, and the top layer is the minimum crater region with a width and height greater than 20 pixels. If the original DEM has a resolution of c , the resolution of the n th layer in the pyramid is $1.2^n \cdot c$ and is recorded to calculate the scaled Haar-like feature classifier. In each layer, a window of 20×20 pixels is slid by a pixel each time to scan the DEM, so the region within the window is classified into crater or non-crater.

We need to detect and delete duplicate crater regions to avoid one crater from being repeatedly counted. When a region in the pyramid is classified as a crater, the rectangular extent on the original DEM, $E = \{x, y, w, h\}$, is stored,

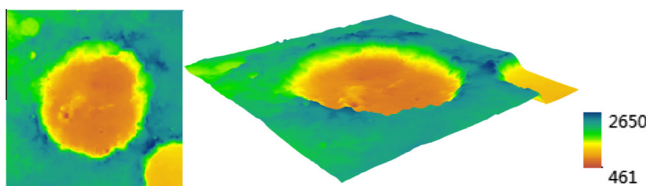


Fig. 5. Examples of positive samples from the DEM rendered in ARCGIS software.

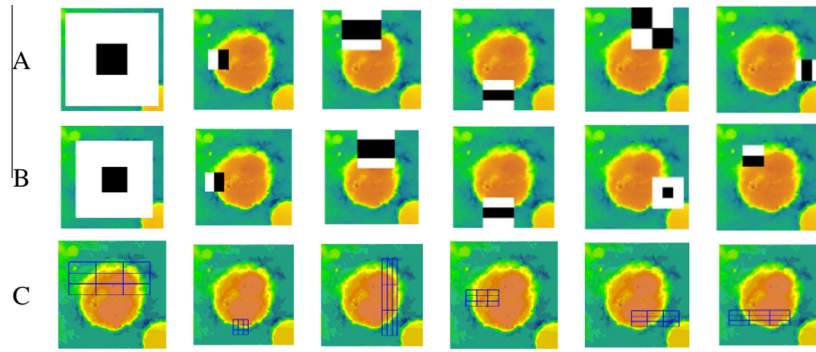


Fig. 6. Top six mask features selected with AdaBoost with the use of the training set. Pictures in rows A, B and C are trained with Haar-like features, scaled Haar-like features and LBP features, respectively.

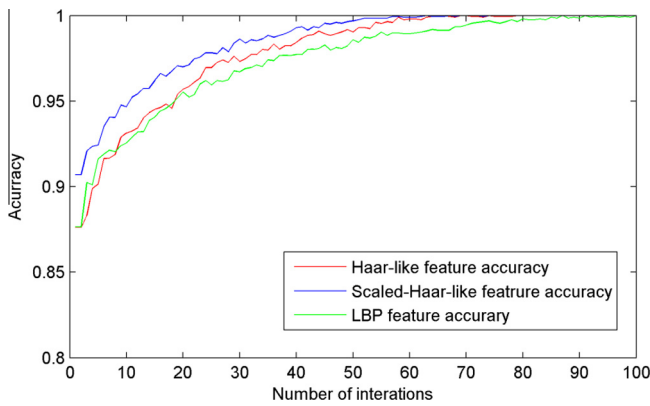


Fig. 7. Accuracy curves of the three classifiers.

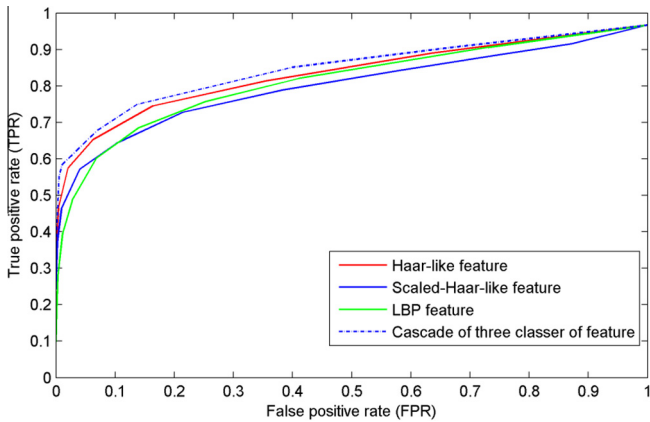


Fig. 8. ROC curves of the three classifiers and the cascade classifier.

where x, y are the coordinates of the top-left corner, and w, h are the width and height of the rectangle. Any two rectangles, E_1 and E_2 , are considered duplicate if they satisfy the following formula:

$$\text{abs}\left(\frac{x_1 + x_1 + w_1}{2} - \frac{x_2 + x_2 + w_2}{2}\right) \leq \frac{\max(w_1, w_2)}{4} \quad (8)$$

$$\text{abs}\left(\frac{y_1 + y_1 + h_1}{2} - \frac{y_2 + y_2 + h_2}{2}\right) \leq \frac{\max(h_1, h_2)}{4} \quad (9)$$

$$\min(w_1, w_2) / \max(w_1, w_2) \geq 0.5 \quad (10)$$

Eqs. (8) and (9) are adopted to detect location closeness, whereas Eq. (10) is employed to detect size similarity. The region with the greater value of classification, R , is kept as the crater region, and the other region is rejected.

4. Delineating crater rims through local terrain analysis and CHT

The crater regions extracted from the classifiers cannot accurately represent the crater rims, and delineating crater rims is an important task in most CDAs. To accomplish this task, we use a method based on terrain analysis, which has been used in imagery data to detect crater rims through texture analysis (Bandeira et al., 2007). We further employ CHT to determine a circle to fit the crater rims and to easily calculate the radius and centre of each detected crater.

4.1. Local terrain analysis

Most impact craters have a negative relief with a circular shape on the planetary surface, and the most dramatic elevation changes can usually be observed around the crater rims. According to simple characteristics, the following steps are performed to determine crater rims:

- (1) With a crater region, a 3×3 mask matrix M is centred over each pixel, E_{rc} , of the original DEM. We calculate the local mean m , and then look for the greatest deviation from m to the minimum (min) or to the maximum (max) of the values in the mask. The value is allocated to the pixel, and new DEM data A are obtained through Eq. (11):

$$A_{rc} = \max[m(M) - \min(M), \max(M) - m(M)] \quad (11)$$

- (2) The value of the threshold T is then calculated, and it can be represented as follows in consideration of the range of values in matrix A :

$$T = \alpha[\max(A) - \min(A)] + \min(A) \quad (12)$$

where α is an empirical value of 0.25.

Next, the threshold T is applied to judge each pixel A_{rc} of matrix A to obtain the value (0 or 1) assigned to each

new pixel B_{rc} in the resulting binary image B . A binary image with only local edges of dramatic elevation changes is then generated by this method. A morphological closing operation with a 3×3 structuring element is then performed to smooth the edges and eliminate small holes in B . With the application of a thinning operation to B , all lines are decreased to single pixel thickness, and the remaining pixels are regarded as the rims of the craters. The thinned binary image B_{th} is taken as the input in the CHT algorithm in the next step.

4.2. CHT

CHT is a common strategy to find circles in images, with a number of algorithms used in the implementation (Yuen et al., 1990; Atherton and Kerbyson, 1999). Generally, most of these algorithms involve three essential steps: accumulator array computation, radius estimation and centre estimation. The goal of CHT is to derive an accumulator array from a binary image, and in the process, the foreground pixels are designated as candidates to cast votes in the accumulator array. The votes of candidate pixels which belong to an image circle tend to accumulate at the accumulator array bin and correspond to the centre of the circle. Our algorithm which determines the crater rims on the basis of on CHT is summarised as follows:

- (1) For a binary image B_{th} with dimensions of $w \times h$ pixels (in our algorithm, the input image is a square image, so w equals h), a 3D accumulator array $A\{w, h, r\}$ is created, and all the cells in the array are initialised to zero. With the assumption that the radius of a crater cannot be smaller than $\frac{1}{4}w$, and the centre of a crater can only appear in an $\frac{1}{2}w \times \frac{1}{2}w$ image block located at the centre of the image, the size of the third dimension for r should satisfy the range of $[\frac{1}{4}w, \frac{1}{2}w]$.

- (2) For each value of r :
All possible circles (with a radius of r) through one certain foreground pixel, $p_{u,v}$, can be determined, and the centres of these circles, $c_{x,y}$, can be simply described in the following mathematical formula:

$$(x - u)^2 + (y - v)^2 = r^2 \quad 0 < x, u < w; 0 < y, v < h \quad (13)$$

where (x, y) and (u, v) are the locations of $c_{x,y}$ and $p_{u,v}$, respectively. Once $c_{x,y}$ is found for one pixel, the value of cell $A(x, y, r)$ is increased by 1.

- (3) After the maximum cell $A(X, Y, R)$ in the accumulator array is found, the circle centred at pixel $p_{X,Y}$ with a radius of R is regarded as the crater rim in the crater region.

The main problems of a large storage space and a long computation time in CHT are non-existent in our approach because the classifiers have filtered out most of the

non-crater areas, and the extracted regions have limited sizes. Finding only the most probable circle in each binary image avoids setting a threshold when peaks are detected in an accumulator array. This process is difficult to decide on if the context of the image is complex. An example of delineated crater rims is shown in Fig. 9. Notably, more than one crater exists in the input region at times, but only the largest one located in the region centre is extracted by the classifier. The other craters are ignored by our method, so only the rim of the main crater is delineated. In this example, the smaller craters can be extracted in smaller detection regions. Therefore, the overlapped craters can be effectively detected by our CDA.

5. Experimental results and discussion

Three sites (Fig. 1) are utilised to test our crater detection method. Fig. 10 shows the three DEMs of the three sites rendered as greyscale images. Site 1 is located around the Herschel crater and is exactly the same as the test site in Bue's method (Bue and Stepinski, 2007). A comparison of the two methods can then be performed. Considering site 1 is also the training sample region, we selected two other regions (sites 2 and 3) which have no training data to validate the effectiveness of our method. Site 2, located around the Huygens crater, has a similar crater distribution as site 1. The two sites are challenging because they are densely distributed, overlapped and heavily degraded craters. Site 3 is located in the south of Valles Marineris with a less complex crater distribution compared with the other two sites. Additional information about the three test sites is shown in Table 1. Note that the column 'Crater count in the Robbins catalogue' in Table 1 counts the craters entirely located within the boundaries of each site. Like all other CDAs, the detection performance of our method is affected by the crater distribution complexity of the area; it will get better quality factors if the craters in the area are well preserved, less overlapped and modified, as shown in the following experimental results.

We used the quality factors of detection percentage $D = 100TP/(TP + FN)$, branching factor $B = FP/TP$ and quality percentage $Q = 100TP/(TP + FP + FN)$ developed by Shufelt (1999) and are used in many other CDAs to evaluate the performance of our method (Barata et al., 2004; Kim et al., 2005; Bue and Stepinski, 2007; Bandeira et al., 2012). TP stands for the number of true positive detections (detected craters are real craters), FP stands for the number of false positive detections (detected craters are not actual craters), and FN stands for the number of false negative detections (undetected real craters). The D parameter can be treated as a measurement of crater-detection performance (larger is better), B can be treated as a measurement of delineation performance (smaller is better), and Q can be treated as a measurement of the overall algorithm performance (larger is better). In our experiments, the latest Robbins catalogue (Robbins and Hynke, 2012) is adopted as the ground truth to calculate

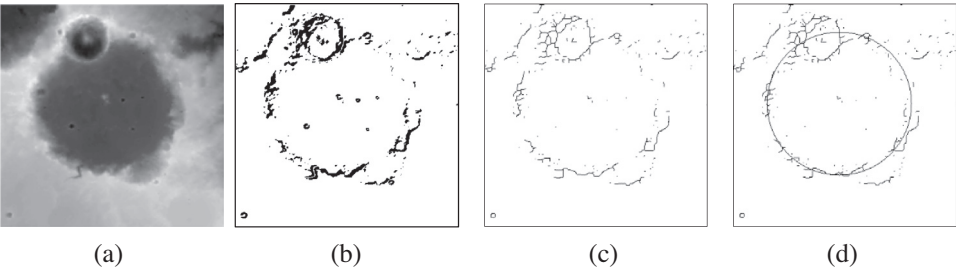


Fig. 9. Results of the delineated crater rims. (a) An input crater region obtained by classification. (b) A binary image generated by local terrain analysis. (c) A thinned binary image. (d) A circle found in the thinned binary image with the use of CHT.

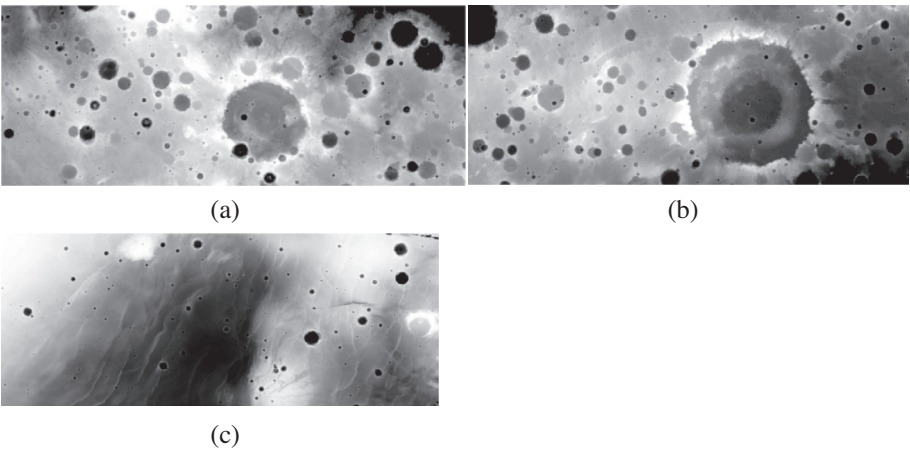


Fig. 10. Topographic data of sites 1, 2 and 3 rendered as greyscale images.

Table 1
Information on the three test sites.

	Top	Bottom	Left	Right	Data block size	Crater count in the Robbins catalogue	Area (km ²)
Site 1	7.58°S	18.42°S	114°E	142°E	3585 × 1388	5027	1,066,414
Site 2	8.05°S	18.89°S	37.69°E	65.69°E	3583 × 1386	4150	1,066,462
Site 3	14.85°S	25.69°S	88.87°W	61.26°W	3534 × 1386	2691	1,051,472

Table 2
Statistics of crater detection results at the three test sites.

	Craters in the Robbins catalogue	Craters $D \geq 6$ km	Craters correctly detected (TP)	Matched craters $D \geq 6$ km	Matched craters $D \geq 6$ km	Craters omitted (FN)	Craters falsely detected (FP)	D (%)	B	Q (%)
Site 1	5027	499	418	367	51	132	66	76	0.16	68
Site 2	4150	389	340	281	59	108	46	76	0.14	69
Site 3	2691	138	176	118	58	20	27	90	0.15	79

the factors for performance evaluation. Because craters with diameters larger than 6 km are treated as positive samples, the craters in the Robbins catalogue satisfying this condition are taken as the ground truth catalogue, as well as the small craters correctly detected by our method. The criteria of detecting duplicate craters (Section 3.3) are employed to match a detected crater to a crater in the ground truth catalogue. The results of the three test sites are shown in Table 2 and Fig. 11.

The performance of our method in the three test sites is different. Site 1 is a challenging site for the crater-detection

algorithm because of the wide range of crater sizes, huge degradation degrees and overlapping geometries. The performance factors for our method in this site are $D = 76\%$, $B = 0.16$ and $Q = 68\%$. Comparison with the factors ($D = 74\%$ $B = 0.29$ and $Q = 61\%$) in Bue’s CDA (Bue and Stepinski, 2007) for the same region shows that factors D and Q for our method are slightly better than that for Bue’s, and factor B has a significant improvement in our CDA. The results indicate that our method can efficiently decrease the false detection rate while maintaining a high detection rate. The crater distribution in site 2 is

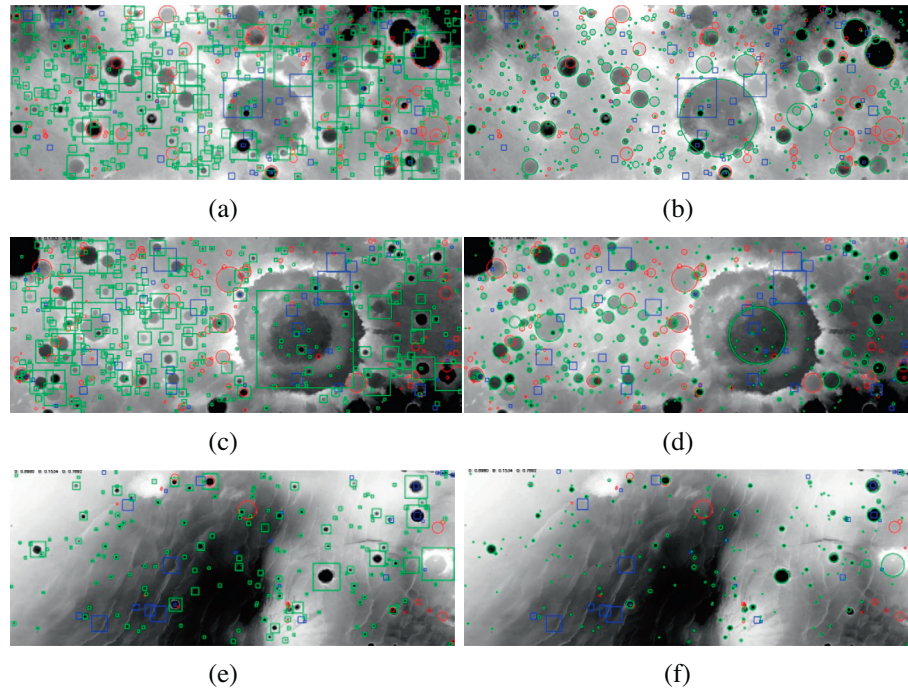


Fig. 11. Crater detection results. (a), (c) and (e) show the crater regions detected by the cascade classifier. (b), (d) and (f) show the results of the delineated crater rims. Green rectangles and circles represent correctly detected craters, blue rectangles are false positive regions and red circles are false negative craters in the ground truth catalogue.

similar to that in site 1, and the factors in these two sites are also similar: $D = 76\%$, $B = 0.14$ and $Q = 69\%$. In site 3, our method has a very impressive performance with $D = 90\%$, $B = 0.15$ and $Q = 79\%$. Therefore, the TP is significantly increased, whereas FP is almost unchanged. This scenario results from the quite sparse distribution of the craters with less degradation and less overlapping in site 3. It is worth noting that the results of other CDAs (Bue and Stepinski, 2007; Stepinski et al., 2009) for the same data source are compared with those of the Barlow catalogue (Barlow, 1988), which was the earliest version of Martian craters but less complete than Robbins catalogue.

Adjusting the threshold T of the classifiers changes the TPR and FPR. Restraining the evaluation factor B at around 0.15 cannot extract several craters with our method. Most of these craters are deeply degraded and modified craters which are rejected by the classifiers, and a small number are overlapped craters mistakenly excluded when deleting duplicate crater regions. This condition will be further investigated in the future. Notably, the smallest crater detected by our CDR is about 8×8 pixels with a 20×20 pixels window. Very small craters cannot be detected by the CDR because the features for the classifier are absent.

6. Conclusions

This study presented a machine learning approach to detect craters on the basis of DEM data. The algorithm constructs AdaBoost classifiers to distinguish craters from

non-craters. We utilise a new scaled Haar-like feature combined with Haar-like and LBP features to enhance the classifiers. The method can delineate crater rims with high accuracy by application of local terrain analysis and CHT on the detected crater regions, which are the output of the classifiers. Experimental results using Mars DEM data show that the method can achieve good performance even in challenging test sites. The performance can even be improved further if the distribution of craters in the site is uncomplicated (i.e. sparse distribution, less degradation and less overlapping). Future research can focus on the improvement of the accuracy and efficiency of the classifier. Furthermore, it would be an interesting topic to compare the performance of crater detection from DEM and imagery and the integration of them. This will be investigated in future research.

Acknowledgements

The authors would like to thank N.G. Barlow, S.J. Robbins and B.M. Hynek for providing the catalogues of Martian impact craters. We also want to thank the anonymous reviewers' insightful and constructive comments. This research was supported by the National Natural Science Foundation of China (Project Nos. 41002120 and 41171355).

References

- Atherton, T.J., Kerbyson, D.J., 1999. Size invariant circle detection. *Image Vision Comput.* 17 (11), 795–803.

- Bandeira, L., Ding, W., Stepinski, T.F., 2012. Detection of sub-kilometer craters in high resolution planetary images using shape and texture features. *Adv. Space Res.* 49 (1), 64–74.
- Bandeira, L.P., Saraiva, J., Pina, P., 2007a. Impact crater recognition on Mars based on a probability volume created by template matching. *IEEE Trans. Geosci. Remote Sens.* 45 (12), 4008–4015.
- Bandeira, L.P., Saraiva, J., Pina, P., 2007b. Development of a methodology for automated crater detection on planetary images. In: Martí, J. et al. (Eds.), *Pattern Recognition and Image Analysis, Lecture Notes in Computer Science*, vol. 4477. Springer, Berlin/Heidelberg, pp. 193–200.
- Barata, T., Alves, E.I., Saraiva, J., Pina, P., 2004. Automatic recognition of impact craters on the surface of Mars. In: Campiño, A., Kamel, M. (Eds.), *Image Analysis and Recognition, Lecture Notes in Computer Science*, vol. 3212. Springer, Berlin/Heidelberg, pp. 489–496.
- Barlow, N.G., 1988. Crater size-frequency distributions and a revised Martian relative chronology. *Icarus* 75 (2), 285–305.
- Bue, B.D., Stepinski, T.F., 2007. Machine detection of Martian impact craters from digital topography data. *IEEE Trans. Geosci. Remote* 45 (1), 265–274.
- Burl, M.C., Stough, T., Colwell, W., Bierhaus, E., Merline, W., Chapman, C., 2001. Automated detection of craters and other geological features. In: *Proceedings of the Sixth International Symposium on Artificial Intelligence and Robotics & Automation in Space*, Montreal, Quebec, Canada, pp. 18–22.
- Cheng, Y., Johnson, A.E., Matthies, L.H., Olson, C.F., 2003. Optical landmark detection for spacecraft navigation. In: *Proceedings of the 13th Annual AAS/AIAA Space Flight Mechanics Meeting*, Ponce, Puerto Rico, AAS 02-224, pp. 1-19.
- Cohen, J.P., Ding, W., in press. Crater detection via genetic search methods to reduce image features. *Adv. Space Res.*
- Costard, F.M., 1989. The spatial distribution of volatiles in the Martian hydrolithosphere. *Earth Moon Planets* 45 (3), 265–290.
- Ding, W., Stepinski, T.F., Mu, Y., et al., 2011. Subkilometer crater discovery with boosting and transfer learning. *ACM Trans. Intell. Syst. Technol. (TIST)* 2 (4), 39.
- Fawcett, T., 2004. Roc graphs: notes and practical considerations for researchers. Technical report, Tech Report HPL-2003-4, HP Laboratories.
- Flores-Méndez, A., 2003. Crater marking and classification using computer vision. In: Sanfeliu, A., Ruiz-Shulcloper, J. (Eds.), *Progress in Pattern Recognition, Speech and Image Analysis, Lecture Notes in Computer Science*, vol. 2905. Springer, Berlin/Heidelberg, pp. 79–86.
- Hartmann, W.K., Neukum, G., 2001. Cratering chronology and the evolution of Mars. *Space Sci. Rev.* 96 (1–4), 165–194.
- Haruyama, J., Ohtake, M., Matsunaga, T., et al., 2009. Long-lived volcanism on the lunar farside revealed by SELENE terrain camera. *Science* 323, 905–908.
- Honda, R., Iijima, Y., Konishi, O., 2002. Mining of topographic feature from heterogeneous imagery and its application to lunar craters. In: Arikawa, S., Shinohara, A. (Eds.), *Progress in Discovery Science, Lecture Notes in Computer Science*, vol. 2281. Springer, Berlin/Heidelberg, pp. 395–407.
- Honda, R., Konishi, O., Azuma, R., Yokogawa, H., Yamanaka, S., Iijima, Y., 2000. Data mining system for planetary images-crater detection and categorization. In: *Proceedings of the International Workshop on Machine Learning of Spatial Knowledge in conjunction with ICML*, Stanford, CA, pp. 103–108.
- Kim, J.R., Muller, J., van Gasselt, S., Morley, J.G., Neukum, G., 2005. Automated crater detection, a new tool for Mars cartography and chronology. *Photogramm. Eng. Remote Sens.* 71 (10), 1205–1217.
- Kuzmin, R., Bobina, N., Zabalueva, E., Shashkina, V., 1989. Structural inhomogeneities of the Martian cryolithosphere. *Sol. Syst. Res.* 22 (3), 121.
- Luo, L., Wang, X., Ji, W., Li, C., 2011. Automated detection of lunar craters based on Chang'E-1 CCD data. In: *The Fourth International Congress on Image and Signal Processing*, vol. 2, Shanghai, pp. 883–887.
- Liao, S., Zhu, X., Lei, Z., Zhang, L., Li, S., 2007. Learning multi-scale block local binary patterns for face recognition. In: Lee, S.-W., Li, S.Z. (Eds.), *Advances in Biometrics, Lecture Notes in Computer Science*, vol. 4642. Springer, Berlin/Heidelberg, pp. 828–837.
- Luo, L., Mu, L., Wang, X., Li, C., Ji, W., Zhao, J., Cai, H., 2013. Global detection of large lunar craters based on the CE-1 digital elevation model. *Front. Earth Sci.* 7 (4), 456–464.
- Magee, M., Chapman, C., Dellenback, S., Enke, B., Merline, W., Rigney, M., 2003. Automated identification of Martian craters using image processing. In: *34th Lunar and Planetary Science Conference*, League City, TX, Abst. #1756.
- Martins, R., Pina, P., Marques, J.S., Silveira, M., 2009. Crater detection by a boosting approach. *IEEE Geosci. Remote Sens. Lett.* 6 (1), 127–131.
- Meng, D., Yunfeng, C., Qingxian, W., 2013. Novel approach of crater detection by crater candidate region selection and matrix-pattern-oriented least squares support vector machine. *Chin. J. Aeronaut.* 26 (2), 385–393.
- Morota, T., Haruyama, J., Honda, C., 2009. Mare volcanism in the lunar farside Moscoviense region: implication for lateral variation in magma production of the Moon. *Geophys. Res. Lett.* 36.
- Ojala, T., Pietikäinen, M., Harwood, D., 1996. A comparative study of texture measures with classification based on featured distributions. *Pattern Recognit.* 29 (1), 51–59.
- Ojala, T., Pietikäinen, M., Harwood, D., 1994. Performance evaluation of texture measures with classification based on Kullback discrimination of distributions. *Pattern Recognition, Conference A: Computer Vision & Image Processing*. In: *Proceedings of the 12th IAPR International Conference*, Jerusalem, vol. 1, pp. 582–585.
- Ojala, T., Pietikäinen, M., Maenpää, T., 2002. Multiresolution gray-scale and rotation invariant texture classification with local binary patterns. *IEEE Trans. Pattern Anal. Mach. Intell.* 24 (7), 971–987.
- Robbins, S.J., Hynek, B.M., 2012. A new global database of Mars impact craters ≥ 1 km. 1: Database creation, properties, and parameters. *J. Geophys. Res.* 117 (E5). <http://dx.doi.org/10.1029/2011JE003966>.
- Rodionova, F.J., Dekhtyareva, K.I., Khamchikhin, A.A., Michael, G.G., Ajukov, S.V., Pugacheva, S.G., Shevchenko, V.V., 2000. Morphological catalogue of the craters of Mars, in: ESA-ESTEC.
- Salamunicar, G., Lončarić, S., 2010. Method for crater detection from Martian digital topography data using gradient value/orientation, morphometry, vote analysis, slip tuning, and calibration. *IEEE Trans. Geosci. Remote Sens.* 48, 2317–2329.
- Salamunićar, G., Lončarić, S., 2008a. GT-57633 catalogue of Martian impact craters developed for evaluation of crater detection algorithms. *Planet. Space Sci.* 56, 1992–2008.
- Salamunićar, G., Lončarić, S., 2008b. Open framework for objective evaluation of crater detection algorithms with first test-field subsystem based on MOLA data. *Adv. Space Res.* 42, 6–19.
- Salamunićar, G., Lončarić, S., Grumpe, A., Wöhler, C., in press. Hybrid method for crater detection based on topography reconstruction from optical images and the new LU78287GT catalogue of Lunar impact craters. *Adv. Space Res.*
- Salamunićar, G., Lončarić, S., Pina, P., Bandeira, L., Saraiva, J., 2011. MA130301GT catalogue of Martian impact craters and advanced evaluation of crater detection algorithms using diverse topography and image datasets. *Planet. Space Sci.* 59, 111–131.
- Sawabe, Y., Matsunaga, T., Rokugawa, S., 2006. Automated detection and classification of lunar craters using multiple approaches. *Adv. Space Res.* 37, 21–27.
- Shufelt, J.A., 1999. Performance evaluation and analysis of monocular building extraction from aerial imagery. *IEEE Trans. Pattern Anal. Mach. Intell.* 21 (4), 311–326.
- Stepinski, T., Ding, W., Vilalta, R., 2012. Detecting impact craters in planetary images using machine learning. In: Magdalena-Benedito, Rafael et al. (Eds.), *Intelligent Data Analysis for Real-Life Applications: Theory and Practice*. IGI Global, Hershey, PA, pp. 146–159.

- Stepinski, T.F., Mendenhall, M., Bue, B., 2007. Robust automated identification of Martian impact craters. Lunar and Planetary Institute Science Conference, Abst. #1338.
- Stepinski, T.F., Mendenhall, M.P., Bue, B.D., 2009. Machine cataloging of impact craters on Mars. *Icarus* 203 (1), 77–87.
- Tanaka, K.L., 1986. The stratigraphy of Mars. *J. Geophys. Res.: Solid Earth* (1978–2012) 91 (B13), E139–E158.
- Urbach, E.R., 2007. Classification of objects consisting of multiple segments with application to crater detection. In: *Proceedings of Eighth International Symposium on Mathematical Morphology*, Rio de Janeiro, Brazil, pp. 81–82.
- Urbach, E.R., Stepinski, T.F., 2009. Automatic detection of sub-km craters in high resolution planetary images. *Planet. Space Sci.* 57 (7), 880–887.
- Vezhnevets, A. GML Adaboost matlab toolbox. Available at: <http://graphics.cs.msu.ru/ru/science/research/machinelearning/adaboost-toolbox> (accessed on 2, 2009).
- Vinogradova, T., Burl, M., Mjolsness, E., 2002. Training of a crater detection algorithm for Mars crater imagery. In: *IEEE Aerospace Conference, Big Sky, MT*, vol. 7, pp. 3201–3211.
- Viola, P., Jones, M., 2001. Rapid object detection using a boosted cascade of simple features. In: *Proceedings of the 2001 IEEE Computer Society Conference on Computer Vision and Pattern Recognition*, vol. 1, pp. I-511–I-518.
- Viola, P., Jones, M.J., 2004. Robust real-time face detection. *Int. J. Comput. Vision* 57 (2), 137–154.
- Wan, C., Cheng, W., Zhou, Z., Zhao, S., Xia, Y., 2012. Automatic extraction of lunar impact craters from Chang'E-1 satellite photographs. *Sci. China Phys. Mech.* 55 (1), 162–169.
- Wetzler, P.G., Honda, R., Enke, B., Merline, W.J., Chapman, C.R., Burl, M.C., 2005. Learning to detect small impact craters. In: *Seventh IEEE Workshops on Application of Computer Vision*, Breckenridge, CO, pp. 178–184.
- Yue, S., He, L., Wen, Y., Lu, G., Lin, H., 2013. Shape characteristics-based extraction of lunar impact craters: using DEM from the Chang'E-1 satellite as a data source. *Ann. GIS* 19 (1), 53–62.
- Yue, Z., Liu, J., Wu, G., 2008. Automated detection of lunar craters based on object-oriented approach. *Chin. Sci. Bull.* 53 (22), 3699–3704.
- Yuen, H.K., Princen, J., Illingworth, J., Kittler, J., 1990. Comparative study of Hough transform methods for circle finding. *Image Vision Comput.* 8 (1), 71–77.
- Zhang, G., Huang, X., Li, S.Z., Wang, Y., Wu, X., 2005. Boosting local binary pattern (LBP)-based face recognition. In: *Advances in Biometric Person Authentication*. *Lecture Notes in Computer Science*, vol. 3338. Springer, Berlin/Heidelberg, pp. 179–186.